Anharmonicity of soft optical phonons as the origin of low lattice thermal conductivity in SrAgSb

Honghao Yao,[1,2] Chen Chen,[3] Feng Cao,[4] Jun Mao,[1] Xingjun Liu,[1] Qian Zhang,[1,*] and Xi Lin[1,2,†]

[1]*School of Materials Science and Engineering, and Institute of Materials Genome & Big Data, Harbin Institute of Technology, Shenzhen 518055, People's Republic of China*

[2]*Blockchain Development and Research Institute, Harbin Institute of Technology, Shenzhen 518055, People's Republic of China*

[3]*School of Physical Sciences, Great Bay University, Dongguan 523000, People's Republic of China*

[4]*School of Science, Harbin Institute of Technology, Shenzhen 518055, People's Republic of China*

(Received 30 August 2023; revised 26 October 2023; accepted 13 November 2023; published 29 November 2023)

Developing materials with low thermal conductivity requires an understanding of phonon transport, and it is of significance for practical applications such as thermoelectrics. Traditionally, weak chemical bonding, heavier atomic masses, and complex structure are the most common features in high-performance thermoelectric materials with low thermal conductivity. In this work, we applied the *ab initio* phonon Boltzmann transport method to investigate the abnormally low lattice thermal conductivity observed in the Zintl-phase compound, SrAgSb, among BaCuSb, SrCuSb, and the isomorphism heavier BaAgSb. The optical-acoustic branches coupling is considered the main reason for the diminishing thermal conductivity of SrAgSb, whereas one low-energy optical branch with low and negative Grüneisen parameters. The hybridization between optical and acoustic branches plays an essential role as the scattering center in reciprocal space, like defects in the crystal lattice. Our analysis illustrates that the soft and anharmonic lowest-lying optical mode contributes to the lower thermal conductivity of SrAgSb and suggests more potential chances for achieving high thermoelectric performance with intrinsic low κ_{lat} among abundant Zintl-phase compounds.

DOI: 10.1103/PhysRevB.108.195206

I. INTRODUCTION

Thermoelectric (TE) properties of materials have attracted great interests in both fundamental science and practical applications because heat can be directly converted into electricity for waste-heat recovery, and vice versa for refrigeration. The dimensionless figure of merit $zT = S^2\sigma T/(\kappa e + \kappa lat)$ is used to index the efficiency of TE materials. Here, T is the temperature, σ is the electrical conductivity, S is the Seebeck coefficient specifying the perturbation-response cross effects between the thermal and electric degrees of freedom, and finally the thermal conductivity consists of the the electronic contribution κ_e and lattice vibration portion κ_{lat}. Since tuning one of these thermal, electric, and cross terms would inevitably affect the others, the optimal figure of merit zT values generally favor a compromised charge-carrier concentration around 10^{19}-10^{20} cm^{-3} in these TE materials [1]. Nevertheless, the lattice thermal conductivity κ_{L} seems to be the only property in the zT expression that might be adjusted independently.

The common strategy of reducing the lattice thermal conductivity requires the defect engineering [2–7] via the introduction of point defects, dislocations, nanostructures, and so on. But, these extrinsic defects would inevitably disturb the electronic transport as well. In addition to such "trial-and-error" experiments, one alternative approach is to use the first-principles density-functional theory (DFT) to computationally examine intrinsic low-κ_{L} mechanisms, successful examples of which include the reported rattlinglike behaviors [8], high-order phonon scattering [9,10], and hierarchy structure [11–14], linear triatomic resonant bonds [15], antibonding from $p-d$ hybridization [16], metavalent bonding [17], and a few others.

Recently, Zintl-phase compounds with ZrBeSi-type structure have received wide attention as promising thermoelectric materials [18–27]. Due to the planar honeycomb layer [28], higher hole-carrier mobility was found among other hierarchical TE materials, ensuring their high electronic properties. The low thermal conductivity with point-defect and grain-boundary scattering further provide some ZrBeSi-type semiconductors with good performance, such as SrAgSb [25], BaAgSb [27,28], and BaAgAs [20]. In addition, the semimetallic BaAgBi also owns favorable thermoelectric performance due to the asymmetric band shape between the Fermi level [18].

Intriguingly, based on the experimental data [20,25], we noticed that the thermal conductivity of SrAgSb is evidently lower than the heavier isomorph, BaAgSb. Based on the classical concepts [29], the phonon features should be similar in the same crystal structure, and κ_{lat} varies with the element monotonically, such as averaged atomic masses. This abnormal inverse κ_{lat} relationship has not been discussed and explained clearly yet [30]. Without exception, lower sound velocity and strong lattice anharmonic are responsible for lower κ_{lat} of BaAgSb [20] and BaAgBi [18]. Understanding this abnormal thermal conductivity could bring insight into

*zhangqf@hit.edu.cn
†linxi@hit.edu.cn

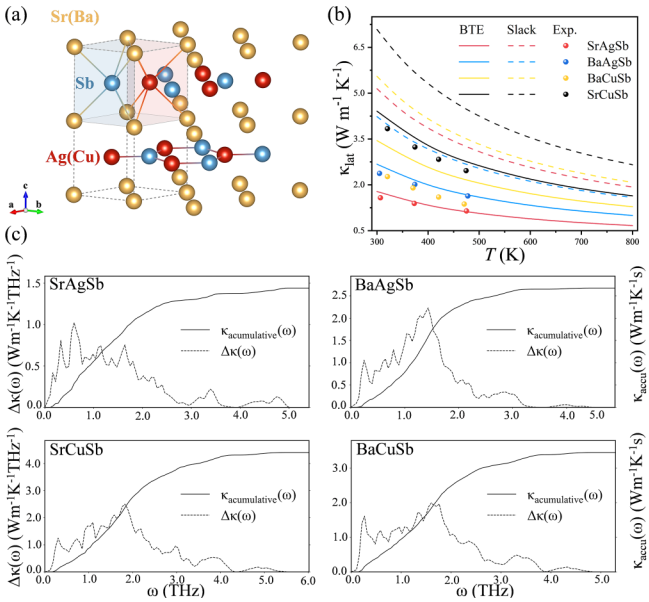

FIG. 1. (a) Crystal structure of ZrBeSi-type compound with $SbSr_6$ ($AgSr_6$) triangular prism and AgSb honeycomb layer as ball-stick model shown. (b) Experimental lattice thermal conductivity for SrAgSb [25], BaAgSb [27], BaCuSb [36], and SrCuSb [36] in comparison with calculated values by phonon Boltzmann transport equation (solid lines) and Slack model (dash lines) (c) The frequency cumulative (solid line) and derivative (dashed line) lattice thermal conductivity from PBTE results.

thermal transport, which promote the ZrBeSi-type TE semiconductor and further benefit the development of other low thermal conductivity materials [31,32].

II. RESULTS AND DISCUSSION

The crystalline structures of the SrAgSb isomorphisms belong to the space group of $P6_3/mmc$ [33], in which the honeycomb Ag-Sb (or Cu-Sb) layer is packed alternately with the alkaline-earth Sr (or Ba) metals layer as shown in Fig. 1(a). The anionic layer is good for electron transport, and the alkaline-earth metals are responsible for phonon scattering. This electron-crystal phonon-glass structure ensures the low lattice thermal conductivity of SrAgSb, SrCuSb, BaAgSb, and BaCuSb [25,27], as presented in Fig. 1(b). In particular, SrAgSb has the lowest κ_L and is much lower than that of others, including BaAgSb, which has a heavier atom.

According to the classical Slack model [34], materials with high average atomic mass often exhibit lower lattice thermal conductivity when heat is carried by phonon above the Debye temperature. The relationship of κ_{lat} by the Slack model, as dashed lines show in Fig. 1(b), are much higher than the experimental data. What is more, it cannot explain the lowest κ_{lat} of SrAgSb. Table I shows the calculated properties of the Slack model. The direct factors of lower κ_{lat} are the low sound speed and strong anharmonicity. Nevertheless, the calculated values in Table I seem unable to explain the inverse relationship of thermal conductivity.

Ab initio phonon Boltzmann transport equation was employed to compared with the experimental data as presented

TABLE I. Calculated thermal properties for empirical Slack model: longitudinal and transversal sound velocities, Grüneisen constant, volume, and Debye temperature.

	BaAgSb	SrAgSb	BaCuSb	SrCuSb
v_L (m/s)	3668	3818	3845	4255
v_T (m/s)	1990	1989	2235	2360
Γ	1.61	1.47	1.57	1.48
V (Å^3)	196.49	174.68	179.09	159.77
Θ (K)	206.63	215.36	238.04	254.46

in Fig. 1(b) (solid lines). And, the direct components of κ_L along the crystal axis are shown in Fig. S1 [35]. The slight deviation in ambient temperature might come from the extra phonon scattering from defects. It is worth noting that the calculated results indicate the lowest lattice thermal conductivity in SrAgSb, which is consistent with the experimental results.

The frequency contribution to κ_{lat} of all compounds at 300 K is shown in Fig. 1(c). The frequency accumulative (solid line) and differential (dashed line) κ_{lat} are calculated. Their dominant contributions are centrally distributed in the low-frequency region since high-energy phonons has lower velocity and less excitation number obeying the Bose-Einstein distribution function. In spite of higher sound speed and more excitation number, acoustic phonons near zero THz carry lower energies and fewer phonon states. Therefore, the frequency of phonons with majority contribution (∼80%) to κ_{lat} of BaAgSb is in the range of 0.5 ∼ 2.2 THz, where it is in the broader range of 0.4 ∼ 2.7 THz for SrAgSb. The extreme points of differential κ_{lat} of BaAgSb, SrCuSb, and BaCuSb are located around 1.4, 1.8, and 1.7 THz, correspondingly. In contrast, the highest peak of SrAgSb is at about 0.6 THz. The following platformlike area fluctuates up and down until 1.6 THz, making its majority κ_L contribution zone broader. However, the median of accumulative κ_{lat} is similar between SrAgSb and BaAgSb, both at around 1.3 THz. The wider platformlike area with much lower κ_L contribution and the similar location of the κ_{lat} median indicates that the dominant κ_L contribution zone in SrAgSb could be more strongly inhibited than others. Therefore, the suspected truncated part of the derivative spectrum around 0.6 ∼ 1.6 THz in SrAgSb can mainly contribute to its abrupt low κ_{lat} compared with other analogs.

A comparison of the group velocity is plotted in Fig. S2 [35], and no abrupt decrease of phonons with large velocity is observed in SrAgSb. The direct comparison of group velocity and phonon band between BaAgSb and SrAgSb is shown in Fig. S3 and Fig. S4. As can be seen, the group velocity of the LA modes of SrAgSb is larger than BaAgSb in the range of 1 ∼ 2 THz, which is normally inversely related to average atomic mass. The detailed anharmonic scattering will be discussed in the following.

Figure 2 presents the phonon dispersions of SrAgSb, BaAgSb, SrCuSb, and BaCuSb, respectively. The mode-dependent Grüneisen parameter is also projected on each phonon band. The color map from blue to red indicates the intervals of Grüneisen parameters from −4 to 4. Four high-energy optical branches are on the top. Other optical branches

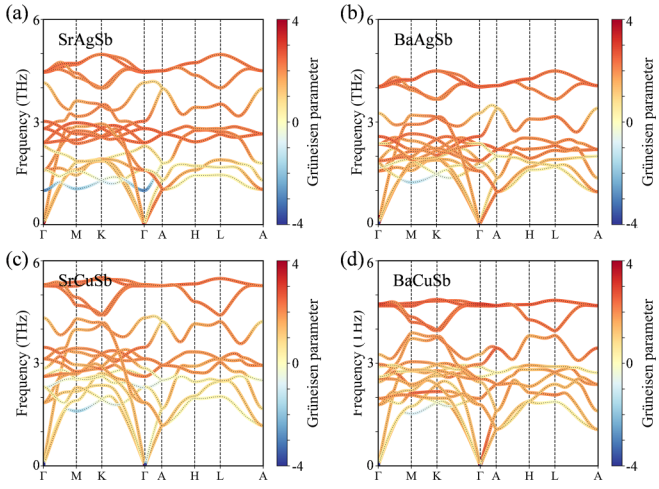

FIG. 2. Calculated phonon band of (a) SrAgSb, (b) BaAgSb, (c) SrCuSb, and (d) BaCuSb. Color smear presents mode Grüneisen parameters, which range from −4 to 4.

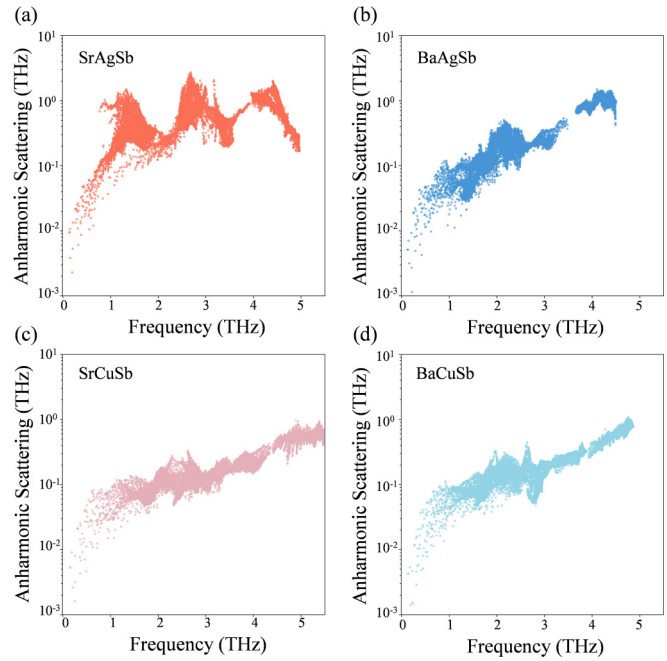

FIG. 3. Mode-dependent anharmonic scattering rate ($\tau_{\omega(\mathbf{q},j)}$) for (a) SrAgSb, (b) BaAgSb, (c)SrCuSb, and (d) BaCuSb.

are densely distributed in the range of 1 ∼ 4 THz. The noteworthy difference between the isostructural compounds is the location of the lowest-lying optical (LLO) branch. The LLO branch of SrAgSb is the lowest, especially at the **M** and **Γ** points, with a minimum frequency of about 1 THz. On the other hand, the LLO branch of SrAgSb shows relatively large anharmonicity with the negative Grüneisen parameter $\gamma_{i,\mathbf{q}}$ and the smallest one is about −3 at the **Γ** point. The negative part of the LLO of SrAgSb extends to about 1.5 THz, whereas the LLO branches of BaAgSb, SrCuSb, and BaCuSb are harder and have less anharmonicity than that of SrAgSb. Their phonon modes both show the negative $\gamma_{i,\mathbf{q}}$ closer to zero nearby the **M** point. When the optical branches become soft, optical-acoustic (OA) phonon hybridization is considered. The softening of optical phonon can be considered as providing more scattering channels [37–39].

The mode-dependent anharmonic scattering rate is plotted in Fig. 3. In SrAgSb, the striking difference is the double prominent peaks compared with others, of which the peaks are located around 1.3 and 2.7 THz, separately. Around the dominant peak of SrAgSb, the corresponding values are one order of magnitude larger than others. The scattering rate is further resolved into two parts, the emission and absorption process in 3-phonon scattering separately in Fig. S5 [35]. After separating the emission and absorption processes, we find that the absorption process is responsible for a large enhancement of the scattering rate around 1.3 THz, whereas the second abrupt peak located around 2.7 THz is from the emission process, which seems to keep away from the ideal main derivative κ_{L} zone from 0.6 to 1.6 THz. Hence, the enhanced scattering rate of 3 phonons is from the absorption process around 1.3 THz, which contributed to the low thermal conductivity of SrAgSb. Note that the front peak of scattering distribution is consistent with the mean location of the soft and anharmonic LLO branch. Therefore, the low κ_{lat} probably should be caused by this unique phonon feature in SrAgSb.

The scattering rate can be qualitatively described by the scattering strength between phonons, as well as the number of allowable scattering channels. The first item is scattering strength, which can be reflected by the Grüneisen parameter [17]. On the other hand, the weighted phase space [37], $W^{\pm}$, is widely used as an indication of the available scattering channels for the 3-phonon process allowed by energy and momentum conservation. The overall weighted phase spaces of BaAgSb and SrAgSb are higher than BaCuSb and SrCuSb, as shown in Fig. S6 [35]. It means that Ag-based compounds own lower κ_{lat} more than expected compared with Cu-based compounds. When the optical branches become soft, the OA phonon hybridization is considered. The softening of optical phonon branches is often treated as an indicator of lower k_{lat} in both calculations [40–43] and experiments [43–46]. The OA phonon hybridization commonly can be considered as providing more scattering channels [38,39]. Notably, similar weighted phase space between SrAgSb and BaAgSb indicates that a single soft optical branch is hard to change the scattering channel significantly. Therefore, the low k_{lat} of SrAgSb could mainly be attributed to the strength of anharmonicity, reflected by the LLO branch with the negative Grüneisen parameter.

Figure 4 presents the anharmonic scattering-rate contour of the absorption process correlated to two initial phonons with ω_{λ} and $\omega_{\lambda'}$. Due to the main effect on heat conduction from the Umklapp process, we extract the Umklapp process, and the sparse $\boldsymbol{q}$ mesh is taken for simplifying postprocessing. The consistency between sparse and dense mesh is checked in Fig. S5. The peak values (pink and red zone) look like an "L" shape in the SrAgSb, as shown in Fig. 4(a), while others are located at the midpoint of the right boundary and appear similarly in Figs. 4(b)–4(d). The L shape can be explained by the fact that the phonon with $\omega_{\lambda'}$ is likely to interact with the soft and anharmonic LLO branch with $\omega_{\lambda'}$ and vice versa. Both lead to the abrupt scattering-rate peak of the absorption process of SrAgSb in Fig. S5(a). Although the optical phonon behaves flat and has a much slower group velocity, the soft and

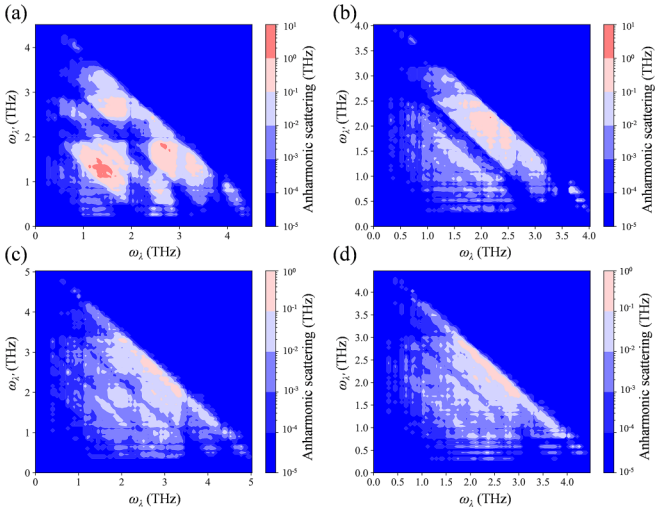

FIG. 4. Mode-dependent anharmonic scattering rate ($\tau_{\omega(\mathbf{q},j)}$) for (a) SrAgSb, (b) BaAgSb, (c) SrCuSb, and (d) BaCuSb in Umklapp and absorption process.

anharmonic LLO branch from 1 to 1.5 THz could dramatically scatter the high group-velocity phonons from 0.6 to 1.6 THz and contribute to the abnormally low κ_L. Although the second abrupt peak of scattering cannot directly diminish the lattice thermal conductivity of SrAgSb, the intensity scattering zones of two 3-phonon processes are related. As shown in Fig. S7 [35], the 2D contour of the emission process of SrAgSb shows that phonon modes around ω_λ ~2.7 THz are more likely to decompose into the zone from 1.3 to 1.4 THz, i.e., the position of the absorption peak. The strong scattering zone of the emission process in SrAgSb looks like a heterochiral L shape. It could be considered as the supplement of $\omega_{\lambda'}$ phonon around 1.3 THz due to the excitation of the absorption process. Both the lower right and left triangles of the absorption and emission process reflect the energy conservation where the third phonon cannot exceed the highest phonon level. Some weakly interacting regions inside the energy-feasible triangle are due to the less phonons state or phonon gap.

To understand the emergence of the negative Grüneisen parameter, we extract the vibrational patterns of the lowest-lying optical modes of SrAgSb at the **Γ** and **M** points, as shown in Fig. S8 [35]. Both cases behave as the bond-angle bending pattern. In the **Γ**-point case, the relative motion between Ag and Sb along the **c** axis and the Sr atom is kept stationary. This vibration pattern, only correlated with the Ag-Sb honeycomb layer, is similar to the "ZO mode" (diatomic transverse oscillation perpendicular to the honeycomb layer) in graphene, of which the Grüneisen parameter is also negative [47–49]. This vibration mode in 2D planar with a bond-bending effect is commonly associated with the negative Grüneisen parameter. In this 3D framework, the overbending ZO mode as 2D counterparts is constrained by the triangular prism framework of Sr-Ag and Sr-Sb. The potential-energy surface is calculated in all compounds with the vibration modes of the ZO mode, as shown in Fig. S9 [35]. The harmonic potential of SrAgSb exhibits the smallest value in all compounds as expected. At the **M** point, the rotational motion is observed, which is similar to the negative thermal expansion materials, like the oxygen-octahedron rotation in the perovskite [50], tetrahedra in zinc blende, and diamondlike semiconductors [51].

We further consider thermal expansion's impact on the phonon band and thermal conductivity of SrAgSb. The uniaxial negative thermal expansion in SrAgSb is identified by using the *ab initio* molecular dynamics (AIMD) method, with "$a(b)$" expanding by 0.5%, and "c" contracting by 0.14%. This anisotropic expansion affects higher-frequency phonons, but has a minimal influence on thermal conductivity as shown in Fig. S10 [35].

III. CONCLUSIONS

In summary, we have calculated the thermal properties of SrAgSb and its isomorphism by the *ab initio* calculations and iteratively solving the phonon Boltzmann equation. The calculated results explain the anomalous trend that SrAgSb owns a lower κ_{lat} (~1.78 W m^{-1} K^{-1} at 300 K) than the heavier BaAgSb (~2.68 W m^{-1} K^{-1} at 300 K). Detailed analysis reveals that this abnormally low κ_{lat} of SrAgSb is due to the soft and anharmonic lower-lying optical branch, scattering the phonons which should assume the primary heat conduction. The negative Grüneisen parameters can be connected with the flexural phonon mode in the planar graphene. The case indicates that the abundant element substitution in one prototype structure have the opportunity to get a soft and anharmonic optical branch easily with no limit of the complex structure. Therefore, a similar scattering effect for thermal conductivity could be evoked in the undiscovered compounds by the element substitution.

IV. EXPERIMENT

A. DFT calculation

The Vienna Ab initio Simulation Package (VASP) [52] is used to perform the first-principles density-functional theory calculations with the Perdew-Burke-Ernzerhof generalized-gradient approximation [53]. The projector augmented-wave [41] method is chosen to represent the atomic pseudopotentials, which ensures fast energy and force convergences with a plane-wave energy cutoff of 500 eV. The k meshes for the primitive cell and the supercell of a size of $4 \times 4 \times 2$ are $8 \times 8 \times 4$ and $2 \times 2 \times 2$, respectively. All the atomic geometries are fully relaxed to the residual forces and stress less than 10^{-4} eV/Å^{-1} and 10^{-3} GPa, respectively. The density-functional perturbation theory [54] is applied to calculate the second-order force-constant matrices and the phonon-dispersion relations [55]. The third-order force constants and anharmonic properties are calculated using the THIRDORDER.PY and SHENGBTE packages [56]. All the crystalline structures are plotted using the VESTA software [57]. The volume changes in 1.5 and −1.5% are applied in Grüneisen calculation. The comparision between experimental and theoretical lattice parameters are listed in Table S1 [35]. The AIMD simulation with the constant pressure and temperature (*NPT* ensemble) is performed to obtain the lattice parameters at 300 K. The running time step is 1 fs with total 10 ps. The AIMD results as shown in Fig. S11 reflect that the system reaches the equilibrium at 300 K [35].

B. Phonon Boltzmann transport equation for lattice thermal conductivity

The SHENGBTE code is used in this work to perform the phonon Boltzmann transport equation (PBTE) based on the first-principles results from the DFT calculations. Under the single relaxation-time approximation, the lattice thermal conductivity tensor along the Cartesian axes of α and β can be iteratively computed as follows:

$$\kappa_{\alpha\beta} = \frac{1}{N_{\mathbf{q}}V}\sum_{\omega(\mathbf{q},j)} C_{\omega(\mathbf{q},j)} v^2_{\omega(\mathbf{q},j)} \tau_{\omega(\mathbf{q},j)}, \tag{1}$$

where $N_{\mathbf{q}}$ is the sampling number within the first Brillouin zone, V is the volume of the unit cell, $C_{\omega(\mathbf{q},j)}$ and $v_{\omega(\mathbf{q},j)}$ are, respectively, the mode-dependent specific heat and group velocity at a specific $\mathbf{q}$ point, and $\tau_{\omega(\mathbf{q},j)}$ is the relaxation time calculated by iteratively solving. Lattice thermal conductivities of many solids computed by using the phonon BTE have been reported widely in the literature [16,58–61].

C. Empirical Slack model for lattice thermal conductivity

In contrast to the PBTE method, the empirical Slack model [34] of lattice thermal conductivity κ_{lat} can also be obtained from the first-principles DFT calculations. The κ_{lat} can be written as

$$\kappa_{\text{lat}} = A[(M\Theta^3\delta)/(\gamma^2 n^{2/3} T)], \tag{2}$$

where M is the average atomic mass, Θ is the acoustic Debye temperature, δ is the averaged volume per atom, γ is the Grüneisen parameter, n is the number of atoms in the primitive cell, T is the temperature, and the coefficient A in general depends on the Grüneisen parameter γ, but can often take an approximated value of 3.1×10^{-6} [62,63]. Note that few quantities can be directly obtained from the DFT phonon-dispersion results. Explicitly, the Debye temperature Θ can be written as

$$\Theta = \frac{h}{kB}\left(\frac{3n}{4\pi V}\right)^{1/3} v_m, \tag{3}$$

where h is the Planck constant, k_B is the Boltzmann constant, V is the unit-cell volume, and the average sound velocity v_m is given in the terms of

$$v_m = \left[\frac{1}{3}\left(\frac{1}{v_{\text{L}}^3} + \frac{2}{v_{\text{T}}^3}\right)\right]^{-1/3}. \tag{4}$$

Here, the transverse and longitudinal wave sound velocities, v_{T} and v_{L}, respectively, are obtained from the group velocity around the Γ point along the crystalline axis. Finally, the Grüneisen constant γ can be sampled within the Brillouin zone as

$$\gamma = \frac{\sum \gamma_{i,q} C_i(q)}{\sum C_i(q)}. \tag{5}$$

where the mode Grüneisen parameter $\gamma_{i,q}$ can be calculated at the small volume-change limit as

$$\gamma_{i,q} = -\frac{\partial \ln \omega_{i,q}}{\partial \ln V}, \tag{6}$$

and the specific heat $C_i(q)$ at each phonon $\omega_{i,q}$ becomes

$$C_i(q) = k_B\left(\frac{\hbar\omega_{i,q}}{k_B T}\right)^2 \frac{\exp(\hbar\omega_{i,q}/k_B T)}{[\exp(\hbar\omega_{i,q}/k_B T) - 1]^2}. \tag{7}$$

ACKNOWLEDGMENTS

This work was funded by the Fund of Science and Technology on Reactor Fuel and Materials Laboratory (Grant No. JCKYS2019201074), the Affiliated Hospital of Putian University, the Guangdong Provincial Key Laboratory of Intelligent Urban Security Monitoring City and Smart Planning (Grant No. GPKLIUSMSCP-2023-KF-01), the National Natural Science Foundation of China (Grants No. 52172194 and No. 51971081), the Natural Science Foundation for Distinguished Young Scholars of Shenzhen (Grant No. RCJC20210609103733073), the Shenzhen Science and Technology Program (Grant No. KQTD20200820113045081), the Fundamental Research Funds for the Central Universities (Grant No. HIT.OCEF.2023048), and the Key Project of Shenzhen Fundamental Research Projects (Grant No. JCYJ20200109113418655).

[1] D. M. Rowe, D. D. Pollock, J. G. Stockholm, R. Taylor, K.-i. Uemura, S. Scherrer, H. Scherrer, B. J. Beaudry, K. Matsuura, T. Kajikawa *et al.*, *CRC Handbook of Thermoelectrics*, 1st ed. (CRC Press, Boca Raton, 1995).

[2] C. Chen, D. Shen, C. Xia, Z. Zhang, W. Wang, Q. Zhang, and Y. Chen, Chem. Eng. J. **441**, 135968 (2022).

[3] H. Wang, H. Hu, N. Man, C. Xiong, Y. Xiao, X. Tan, G. Liu, and J. Jiang, Mater. Today Phys. **16**, 100298 (2021).

[4] H. Deng, X. Lou, W. Lu, J. Zhang, D. Li, S. Li, Q. Zhang, X. Zhang, X. Chen, D. Zhang *et al.*, Nano Energy **81**, 105649 (2021).

[5] Y. Wu, P. Nan, Z. Chen, Z. Zeng, R. Liu, H. Dong, L. Xie, Y. Xiao, Z. Chen, H. Gu *et al.*, Adv. Sci. **7**, 1902628 (2020).

[6] Z. Chen, B. Ge, W. Li, S. Lin, J. Shen, Y. Chang, R. Hanus, G. J. Snyder, and Y. Pei, Nat. Commun. **8**, 13828 (2017).

[7] X. Liang, Phys. Rev. B **95**, 155313 (2017).

[8] T. Tadano and S. Tsuneyuki, Phys. Rev. Lett. **120**, 105901 (2018).

[9] L. Xie, J. H. Feng, R. Li, and J. Q. He, Phys. Rev. Lett. **125**, 245901 (2020).

[10] Y. Tian, S. Jia, R. J. Cava, R. Zhong, J. Schneeloch, G. Gu, and K. S. Burch, Phys. Rev. B **95**, 094104 (2017).

[11] W. Qiu, L. Xi, P. Wei, X. Ke, J. Yang, and W. Zhang, Proc. Natl. Acad. Sci. USA **111**, 15031 (2014).

[12] M. Mukherjee and A. K. Singh, ACS Appl. Mater. Interfaces **12**, 8280 (2020).

[13] K. Pal, J. He, and C. Wolverton, Chem. Mater. **30**, 7760 (2018).

[14] Q. D. Gibson, T. Zhao, L. M. Daniels, H. C. Walker, R. Daou, S. Hébert, M. Zanella, M. S. Dyer, J. B. Claridge, B. Slater *et al.*, Science **373**, 1017 (2021).

[15] J. Ji, Q. Tang, M. Yao, H. Yang, Y. Jin, Y. Zhang, J. Xi, D. J. Singh, J. Yang, and W. Zhang, J. Am. Chem. Soc. **144**, 18552 (2022).

[16] J. He, Y. Xia, W. Lin, K. Pal, Y. Zhu, M. G. Kanatzidis, and C. Wolverton, Adv. Funct. Mater. **32**, 2108532 (2021).

[17] L. Elalfy, D. Music, and M. Hu, Phys. Rev. B **103**, 075203 (2021).

[18] Z. Zhou, K. Peng, S. Xiao, Y. Wei, Q. Dai, X. Lu, G. Wang, and X. Zhou, J. Phys. Chem. Lett. **13**, 2291 (2022).

[19] E. Haque, RSC Adv. **11**, 15486 (2021).

[20] K. Peng, Z. Zhou, H. Wang, H. Wu, J. Ying, G. Han, X. Lu, G. Wang, X. Zhou, and X. Chen, Adv. Funct. Mater. **31**, 2100583 (2021).

[21] S. Chanakian, D. Uhl, D. Neff, F. Drymiotis, J. Park, V. Petkov, A. Zevalkink, and S. Bux, J. Mater. Chem. A **8**, 6004 (2020).

[22] C. Chen, X. Li, W. Xue, F. Bai, Y. Huang, H. Yao, S. Li, Z. Zhang, X. Wang, J. Sui *et al.*, Nano Energy **73**, 104771 (2020).

[23] C. Chen, Z. Feng, H. Yao, F. Cao, B.-H. Lei, Y. Wang, Y. Chen, D. J. Singh, and Q. Zhang, Nat. Commun. **12**, 5718 (2021).

[24] C. Chen, W. Xue, S. Lia, Z. Zhang, X. Li, X. Wang, Y. Liu, J. Sui, X. Liu, F. Cao *et al.*, Proc. Natl. Acad. Sci. USA **116**, 2831 (2019).

[25] W. Zhang, C. Chen, H. Yao, W. Xue, S. Li, F. Bai, Y. Huang, X. Li, X. Lin, F. Cao *et al.*, Chem. Mater. **32**, 6983 (2020).

[26] S.-F. Wang, Z.-G. Zhang, B.-T. Wang, J.-R. Zhang, and F.-W. Wang, Chin. Phys. Lett. **38**, 046301 (2021).

[27] Y. Huang, C. Chen, W. Xue, X. Wang, Y. Liu, H. Yao, Z. Zhang, Y. Chen, F. Cao, X. Liu *et al.*, Sci. China Mater. **64**, 2541 (2021).

[28] S. Zheng, S. Xiao, K. Peng, Y. Pan, X. Yang, X. Lu, G. Han, B. Zhang, Z. Zhou, G. Wang *et al.*, Adv. Mater. **35**, 2210380 (2022).

[29] R. W. Keyes, Phys. Rev. **115**, 564 (1959).

[30] Z. Z. Zhou, K. L. Peng, H. X. Fu, H. Wu, G. Y. Wang, and X. Y. Zhou, Phys. Rev. Appl. **16**, 064034 (2021).

[31] J. Ding, T. Lanigan-Atkins, M. Calderón-Cueva, A. Banerjee, D. L. Abernathy, A. Said, A. Zevalkink, and O. Delaire, Sci. Adv. **7**, eabg1449 (2021).

[32] R. Hanus, J. George, M. Wood, A. Bonkowski, Y. Cheng, D. L. Abernathy, M. E. Manley, G. Hautier, G. J. Snyder, and R. P. Hermann, Mater. Today Phys. **18**, 100344 (2021).

[33] D. K. Wilson, B. Saparov, and S. Bobev, Z. Anorg. Allg. Chem. **637**, 2018 (2011).

[34] G. A. Slack, J. Phys. Chem. Solids **34**, 321 (1973).

[35] See Supplemental Material at http://link.aps.org/supplemental/10.1103/PhysRevB.108.195206 for anisotropic calculated thermal conductivities, group velocities, weight phase spaces, scattering rate distributions in Umklapp and emission processes, vibration mode, potential energy curves, AIMD results, and calculated and experimental lattice parameters. It also contains Refs. [25,27].

[36] S. Zheng, K. Peng, S. Xiao, Z. Zhou, X. Lu, G. Han, B. Zhang, G. Wang, and X. Zhou, J. Adv. Ceram. **11**, 1604 (2022).

[37] W. Li and N. Mingo, Phys. Rev. B **90**, 094302 (2014).

[38] W. Li and N. Mingo, Phys. Rev. B **89**, 184304 (2014).

[39] O. Delaire, J. Ma, K. Marty, A. F. May, M. A. McGuire, M. H. Du, D. J. Singh, A. Podlesnyak, G. Ehlers, M. D. Lumsden *et al.*, Nat. Mater. **10**, 614 (2011).

[40] X. Liu, T. Ouyang, D. Zhang, H. Huang, H. Wang, H. Wang, and Y. Ni, J. Appl. Phys. **127**, 205106 (2020).

[41] Z. Gao, F. Tao, and J. Ren, Nanoscale **10**, 12997 (2018).

[42] A. Hong, Y. Tang, and J. Liu, J. Phys. Chem. C **125**, 24796 (2021).

[43] L. Lindsay, C. Hua, X. L. Ruan, and S. Lee, Mater. Today Phys. **7**, 106 (2018).

[44] H. Yu, G. Huang, Q. Peng, L.-C. Chen, H.-J. Pang, X.-Y. Qin, P.-F. Qiu, X. Shi, L.-D. Chen, and X.-J. Chen, J. Alloys Compd. **822**, 153610 (2020).

[45] Z. Li, S. Li, J.-P. Castellan, R. Heid, Y. Xiao, L.-D. Zhao, Y. Chen, and F. Weber, Phys. Rev. B **105**, 014308 (2022).

[46] H. Liu, J. Yang, X. Shi, S. A. Danilkin, D. Yu, C. Wang, W. Zhang, and L. Chen, J. Materiomics **2**, 187 (2016).

[47] X.-J. Ge, K.-L. Yao, and J.-T. Lü, Phys. Rev. B **94**, 165433 (2016).

[48] N. Mounet and N. Marzari, Phys. Rev. B **71**, 205214 (2005).

[49] Y. Aierken, D. Çakır, C. Sevik, and F. M. Peeters, Phys. Rev. B **92**, 081408(R) (2015).

[50] Y. Fu, L. Wei, H. Zhang, X. Wang, B. Liu, Y. Zhang, X. Lv, J. Zhou, H. Yu, Y. Hu *et al.*, Results Phys. **19**, 103591 (2020).

[51] K. Yang, J. Xiao, J.-W. Luo, S.-S. Li, S.-H. Wei, and H.-X. Deng, New J. Phys. **21**, 123015 (2019).

[52] G. Kresse and J. Furthmüller, Phys. Rev. B **54**, 11169 (1996).

[53] J. P. Perdew, K. Burke, and M. Ernzerhof, Phys. Rev. Lett. **77**, 3865 (1996).

[54] X. Wu, D. Vanderbilt, and D. R. Hamann, Phys. Rev. B **72**, 035105 (2005).

[55] A. Togo and I. Tanaka, Scr. Mater. **108**, 1 (2015).

[56] W. Li, J. Carrete, N. A. Katcho, and N. Mingo, Comput. Phys. Commun. **185**, 1747 (2014).

[57] K. Momma and F. Izumi, J. Appl. Crystallogr. **44**, 1272 (2011).

[58] Y. Zhao, S. Zeng, G. Li, C. Lian, Z. Dai, S. Meng, and J. Ni, Phys. Rev. B **104**, 224304 (2021).

[59] J. He, S. Hao, Y. Xia, S. S. Naghavi, V. Ozoliņš, and C. Wolverton, Chem. Mater. **29**, 2529 (2017).

[60] T. Pandey, C. A. Polanco, L. Lindsay, and D. S. Parker, Phys. Rev. B **95**, 224306 (2017).

[61] N. Wang, M. Li, H. Xiao, X. Zu, and L. Qiao, Phys. Rev. Appl. **13**, 024038 (2020).

[62] L. Dawahre, R. Lu, H. Djieutedjeu, J. Lopez, T. P. Bailey, B. Buchanan, Z. Yin, C. Uher, and P. F. P. Poudeu, ACS Appl. Mater. Interfaces **12**, 44991 (2020).

[63] Z. Hou, Y. Takagiwa, Y. Shinohara, Y. Xu, and K. Tsuda, ACS Appl. Mater. Interfaces **11**, 11545 (2019).